

See discussions, stats, and author profiles for this publication at: <https://www.researchgate.net/publication/263952332>

Origin of photoluminescence and XAFS study of (ZnS) $1-x$ (AgInS₂) x nanocrystals

ARTICLE in JOURNAL OF PHYSICAL CHEMISTRY LETTERS · DECEMBER 2013

Impact Factor: 7.46 · DOI: 10.1021/jz402443y

CITATIONS

13

READS

60

4 AUTHORS, INCLUDING:



Jagadeeswararao Metikoti

Indian Institute of Science Education and Res...

5 PUBLICATIONS 41 CITATIONS

SEE PROFILE



Tomohiro Shibata

Illinois Institute of Technology

70 PUBLICATIONS 827 CITATIONS

SEE PROFILE



Angshuman Nag

Indian Institute of Science Education and Res...

44 PUBLICATIONS 1,497 CITATIONS

SEE PROFILE

Origin of Photoluminescence and XAFS Study of $(\text{ZnS})_{1-x}(\text{AgInS}_2)_x$ Nanocrystals

M. Jagadeeswara Rao,[†] Tomohiro Shibata,^{‡,§} Soma Chattopadhyay,^{‡,§} and Angshuman Nag^{*,†}

[†]Department of Chemistry, Indian Institute of Science Education and Research (IISER), Dr. Homi Bhabha Road, Pune, India 411008

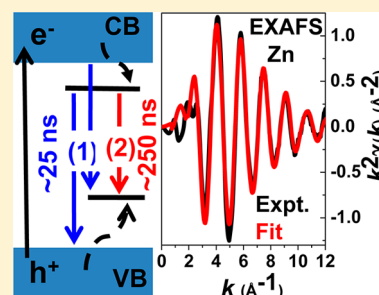
[‡]MRCAT, Sector 10, Argonne National Laboratory, 9700 South Cass Avenue, Bldg 433B, Argonne, Illinois 60439, United States

[§]CSRRI & Department of Physics, Advanced Materials Group, Illinois Institute of Technology, 3300 South Federal Street, Chicago, Illinois 60616, United States

S Supporting Information

ABSTRACT: Donor–Acceptor transition was previously suggested as a mechanism for luminescence in $(\text{ZnS})_{1-x}(\text{AgInS}_2)_x$ nanocrystals. Here we show the participation of delocalized valence/conduction band in the luminescence. Two emission pathways are observed: Path-1 involves transition between a delocalized state and a localized state exhibiting higher energy and shorter lifetime (~ 25 ns) and Path-2 (donor–acceptor) involves two localized defect states exhibiting lower emission energy and longer lifetime (>185 ns). Surprisingly, Path-1 dominates (82% for $x = 0.33$) for nanocrystals with lower x , in sharp difference with prior assignment. Luminescence peak blue shifts systematically by 0.57 eV with decreasing x because of this large contribution from Path-1. X-ray absorption fine structure (XAFS) study of $(\text{ZnS})_{1-x}(\text{AgInS}_2)_x$ nanocrystals shows larger AgS_4 tetrahedra compared with InS_4 tetrahedra with Ag–S and In–S bond lengths 2.52 and 2.45 Å respectively, whereas Zn–S bond length is 2.33 Å along with the absence of second nearest-neighbor Zn–S–metal correlation.

SECTION: Physical Processes in Nanomaterials and Nanostructures



The bandgap of $(\text{ZnS})_{1-x}(\text{AgInS}_2)_x$ solid solution can be tuned throughout the visible range of spectrum, therefore making them suitable for visible light-driven optoelectronic and photocatalytic applications.¹ $(\text{ZnS})_{1-x}(\text{AgInS}_2)_x$ nanocrystals (NCs) are being explored recently for various applications including photovoltaic,^{2–4} photocatalysis,^{5,6} photodetector,⁷ and luminescence.^{8–11} To date, luminescence of $(\text{ZnS})_{1-x}(\text{AgInS}_2)_x$ appears to be the most promising property for application.

Similar to band-edge emission of cadmium-chalcogenide-based NCs,^{12–16} photoluminescence (PL) of $(\text{ZnS})_{1-x}(\text{AgInS}_2)_x$ NCs can be tuned over a wide range of wavelengths (500 to 750 nm), along with high quantum efficiency $\sim 70\%$.^{8,17–19} However, $(\text{ZnS})_{1-x}(\text{AgInS}_2)_x$ NCs exhibit some interesting and intrinsic differences from cadmium chalcogenide NCs: (i) $(\text{ZnS})_{1-x}(\text{AgInS}_2)_x$ is nontoxic, as opposed to cadmium chalcogenide; (ii) $(\text{ZnS})_{1-x}(\text{AgInS}_2)_x$ NCs exhibit large Stokes shift between absorption and emission unlike band-edge emission of CdSe NCs and therefore detrimental self-absorption or nonradiative Forster resonance energy transfer is less probable for $(\text{ZnS})_{1-x}(\text{AgInS}_2)_x$ NCs; and (iii) $(\text{ZnS})_{1-x}(\text{AgInS}_2)_x$ NCs exhibit poorer color purity with larger full-width at half maxima (fwhm ~ 100 nm). Another kind of bright NC emitter is doped NCs, particularly Mn-doped NCs,^{11,20,21} which exhibit large Stokes shift and large fwhm. However, unlike $(\text{ZnS})_{1-x}(\text{AgInS}_2)_x$ NCs, ensembles of Mn-doped NCs typically show PL wavelength fixed around 580 nm, apart from a recent study²² showing the

PL of single (not ensemble) Mn-doped NCs tunable over a wide range. Furthermore, lifetime of Mn-related emission is close to a millisecond, while that of $(\text{ZnS})_{1-x}(\text{AgInS}_2)_x$ NCs is a few hundred nanoseconds. Lower lifetime of $(\text{ZnS})_{1-x}(\text{AgInS}_2)_x$ NCs is advantageous to produce high-efficiency electroluminescence devices.²³

Here we describe the origin of luminescence in $(\text{ZnS})_{1-x}(\text{AgInS}_2)_x$ NCs with $x = 0.33$ to 1 and explore the local structure of these NCs using XAFS. The origin of PL in $(\text{ZnS})_{1-x}(\text{AgInS}_2)_x$ NCs were previously described as donor–acceptor (D–A) transitions involving two localized defect states, where the emission energy can be tuned through a change in the coulomb interaction due to change in the distance between the D–A pair.^{5,6,24,25} $(\text{ZnS})_{1-x}(\text{AgInS}_2)_x$ NCs allow us to tune the band gap simply by varying the composition but without changing the size of NCs and therefore not altering the D–A pair distance. Interestingly, the systematic blue shift in bandgap for decreasing x leads to very similar shift in PL peak, which cannot be explained by the D–A model. Furthermore, the PL shift of 0.57 eV by changing x from 1 to 0.33 is too large compared with D–A pair Coulomb energy. Our PL study shows that the luminescence has two components: (i) a faster (~ 25 ns) transition involving

Received: November 12, 2013

Accepted: December 10, 2013

Published: December 10, 2013



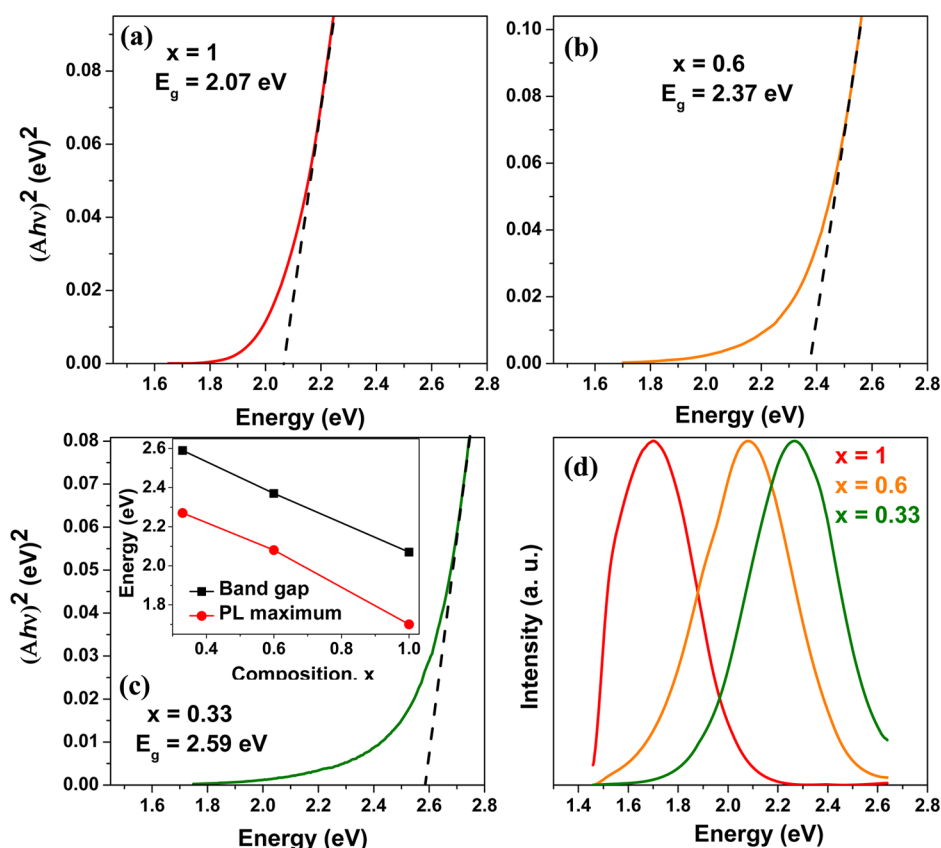


Figure 1. (a–c) UV–visible absorption data plotted as $(Ah\nu)^2$ versus energy for colloidal $(\text{ZnS})_{1-x}(\text{AgInS}_2)_x$ NCs with different x . Black dashed line shows the extrapolation of the linear portion of the plot to $(Ah\nu)^2 = 0$. (d) Photoluminescence (PL) data for colloidal $(\text{ZnS})_{1-x}(\text{AgInS}_2)_x$ NCs with different x after excitation at 2.76 eV (450 nm); all spectra were normalized at their respective maximum intensity. Inset to panel c compares variation in band gap and PL peak position with composition x of $(\text{ZnS})_{1-x}(\text{AgInS}_2)_x$ NCs.

delocalized valence/conduction band and localized defects and (ii) a slower (>185 ns) transition involving localized D–A pairs. The D–A pair contribution decreases drastically with decreasing x , and for $x = 0.33$, the other path, delocalized–localized transition, dominates PL.

The electronic and optical properties depend strongly on the structure and surface chemistry of the NC. These NCs are too small to undergo single-crystal X-ray diffraction (XRD) study, and even the powder XRD peaks broaden, sometimes making it difficult to distinguish between different crystal structures and compositions (homogeneous or heterogeneous).^{26,27} In an effort to gain detailed insight about the local structure of $(\text{ZnS})_{1-x}(\text{AgInS}_2)_x$ NCs, we have performed XAFS study. Unlike XRD, XAFS does not rely on long-range ordering in a crystal. XAFS study on $(\text{ZnS})_{1-x}(\text{AgInS}_2)_x$ NCs shows Ag–S, Zn–S, and In–S bond lengths to be 2.52, 2.33, and 2.45 Å respectively, similar to those in bulk ZnS and AgInS₂, respectively. However, metal–metal second nearest-neighbor correlation is largely absent because of both small size of NCs and random occupation of the cation sites in the solid solution. To the best of our knowledge, XAFS study on $(\text{ZnS})_{1-x}(\text{AgInS}_2)_x$ NCs for all $x > 0$ has not been reported before.

Oleylamine-capped colloidal $(\text{ZnS})_{1-x}(\text{AgInS}_2)_x$ NCs were synthesized following ref 28. Experimental details are given in the Supporting Information (SI). UV–visible absorption spectra show that the optical gap of NCs blue shifts systematically with increase in ZnS content without exhibiting sharp excitonic feature similar to prior reports.^{5,28} The optical

band gap of direct gap semiconductor can be obtained indirectly by using the equation $ah\nu = P(h\nu - E_g)^{1/2}$, where α is the absorption coefficient, $h\nu$ is the photon energy, E_g is the optical band gap, and P is a constant.^{2,29} We can replace α by absorbance A because optical path and concentration of sample are invariant here.⁴ Figure 1a–c showed plots of $(Ah\nu)^2$ versus $h\nu$ for NC samples with different compositions, x . E_g is obtained by extrapolating the linear portion of the plot at $(Ah\nu)^2 = 0$. Band gaps are found to be 2.07, 2.37, and 2.59 eV for NCs with $x = 1$, 0.6 and 0.33, respectively. Band gap of 2.07 eV for AgInS₂ ($x = 1$) NCs is slightly higher than that of bulk AgInS₂ (1.87 eV for orthorhombic phase and 1.98 eV for chalcopyrite phase),³⁰ suggesting quantum confinement effect in our NCs. The sizes of NCs obtained from TEM remain similar (~ 5 nm) for all three NC samples, in accordance with ref 28, suggesting that the change in band gap is because of the change in composition of NCs.

PL spectra (Figure 1d) of colloidal $(\text{ZnS})_{1-x}(\text{AgInS}_2)_x$ NCs exhibit a significant blue shift with increase in ZnS content, similar to absorption spectra. The inset to Figure 1c shows a similar trend in the change of band gap and PL peak position with composition of NCs. However, the origin of PL appears to be different than band-edge emission, exhibiting a large Stokes shift compared with band gap and also a broad fwhm. In fact, the origin of PL in these solid solution NCs has previously been assigned^{6,24,25} to defect-related D–A transitions, which do not involve the valence band maximum and conduction band minimum. Therefore, a similar shift in energy for both band gap and PL peak position is unexpected from D–A model.

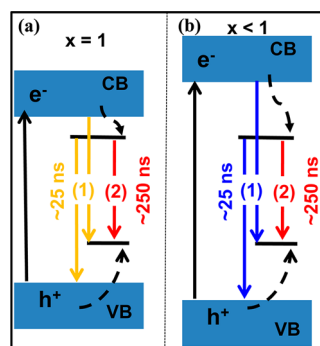


Figure 2. Schematic diagram explaining the luminescence mechanism of $(\text{ZnS})_{1-x}(\text{AgInS}_2)_x$ NCs for (a) $x = 1$ and (b) $x < 1$. Valence band and conduction band systematically moves downward and upward, respectively, with increase in ZnS content; deep midgap defect levels remain largely unaltered. This scenario leads to a systematic blue shift in emission Path-1 depending on the shift in valence/conduction band with decreasing x , but the energy of Path-2 remains unaltered for similar sized NCs.

Figure 2a shows a schematic presentation of possible emission mechanism. Two kinds of defect-related emissions are possible giving large Stokes shift. The first one involves the transition between a delocalized state (valence band maximum or conduction band minimum) and a localized defect state, as indicated by Path-1, and the second one involves the D–A transition between two localized states, indicated as Path-2. The energy of the D–A pair emission is given by²³

$$E = E_g - (E_A + E_D) + e^2/4\pi\epsilon_0\epsilon r$$

where E_A and E_D are respective ionization energy of acceptor and donor, r is the distance between donor and acceptor, e is the electron charge, ϵ is the dielectric constant, and ϵ_0 is the permittivity of vacuum. The last term, $e^2/4\pi\epsilon_0\epsilon r$, accounts for the Coulomb interaction between the donor and acceptor, and smaller r results in higher emission energy. However, the observed shift in PL peak position with composition in Figure 1d is 0.57 eV, which is too high to attribute to Coulomb energy for D–A pairs (~ 0.15 eV for $r \approx 1$ nm, see Table S1 in the SI). Also, a possible change in ϵ with change in composition of NCs will be too small to account for the change in PL energy using D–A pair mechanism.

To distinguish the contributions of two paths in Figure 2a, we prepared $(\text{ZnS})_{1-x}(\text{AgInS}_2)_x$ solid solution NCs where valence/conduction bands shift with composition but the size of NCs remains unchanged, therefore with not much change in the D–A pair distance. Figure 2b shows the schematic energy level diagram for $(\text{ZnS})_{1-x}(\text{AgInS}_2)_x$ ($x < 1$) solid solution NCs in comparison with Figure 2a for AgInS_2 ($x = 1$) NCs. There might be some spread in the energy level of defect states based on composition and local environment; however, for simplicity, we have not altered the defect state energies in both schematics in Figure 2a,b. Because both the size of the NC and hence distance between D–A pairs remain similar for all x , the D–A pair transition (Path-2) energy should not vary much with composition, as opposed to our observation in Figure 1d. Furthermore, the lifetime of Path-2 is also expected to be similar for all compositions because there is no systematic change in the wave function overlap of D–A pairs for similar sized NCs.

Figure 3 shows the PL decay for $(\text{ZnS})_{1-x}(\text{AgInS}_2)_x$ NCs with $x = 1, 0.6$, and 0.33 . The emission energies were fixed at

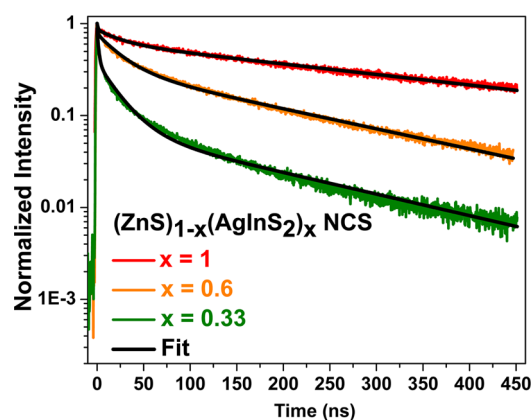


Figure 3. Photoluminescence decay dynamics of colloidal $(\text{ZnS})_{1-x}(\text{AgInS}_2)_x$ NCs for different x , after excitation at 2.7 eV (459 nm). Emission energies were fixed at the peak positions of corresponding steady state spectrum shown in Figure 1d.

Table 1. Best-Fit Parameters of Photoluminescence Decay Profiles of $(\text{ZnS})_{1-x}(\text{AgInS}_2)_x$ Solid Solution NCs in Figure 3 Using Tri-Exponential Decay: $I(t) = a_1 \exp(-t/\tau_1) + a_2 \exp(-t/\tau_2) + a_3 \exp(-t/\tau_3)$

composition (x)	energy (eV)	a_0 (%)	τ_0 (ns)	a_1 (%)	τ_1 (ns)	a_2 (%)	τ_2 (ns)
1	1.70	16	0.9	24	27	60	380
0.6	2.08	11	0.9	52	26	37	199
0.33	2.27	55	1	37	23	8	185

the corresponding emission maxima obtained from Figure 1d. Clearly, the decay becomes faster with decreasing x . These decays can be fitted with three exponentials, and the best-fit parameters are given in Table 1. For all samples, two radiative channels are observed with lifetimes $\tau_1 \approx 25$ ns and $\tau_2 > 185$ ns, similar to previous studies.^{6,10,24} We assign the faster (τ_1) decay to Path-1 (delocalized–localized transitions) and slower (τ_2) decay to Path-2 (localized–localized transition). A subnanosecond ($\tau_0 = \sim 0.9$ ns) decay that typically arises from nonradiative decay channels is also observed, which is more prominent for $x = 0.33$ composition. The amplitude, a_2 for τ_2 (Path-2) sharply decreases with decreasing x . For $x = 1$, Path-2 has 60% contribution in the overall PL decay, which decreases systematically to only 8% for $x = 0.33$, suggesting a minor contribution of D–A transition in the PL for $x = 0.33$. Furthermore, to compare the relative contributions only from radiative processes τ_1 and τ_2 , excluding the nonradiative τ_0 , % values for $a_1/(a_1 + a_2)$ and $a_2/(a_1 + a_2)$ have been extracted from Table 1. It shows that the relative radiative contribution for Path-2, $a_2/(a_1 + a_2)$ in %, systematically decreases from 81% for $x = 1$ to 41% and 18% for $x = 0.6$ and 0.33 , respectively. In contrast, contribution from Path-1 increases from 29% for $x = 1$ to 60% and 82% for $x = 0.6$ and 0.33 , respectively. These data suggest that the light emission for $x = 0.33$ (lower x) has a very minor contribution from the D–A pair transition, in sharp difference with previous reports,^{5,6,24,25} and instead is almost entirely governed by Path-1. This large contribution from Path-1 can explain the similar trend in the change in band gap and PL peak position with different compositions shown in the inset of Figure 1c. Interestingly, the steady-state PL spectra (Figure 1d and ref 28) with intermediate compositions x , having comparable contributions from both emission Paths-1 and -2, also show the possibility of convolution of two broad

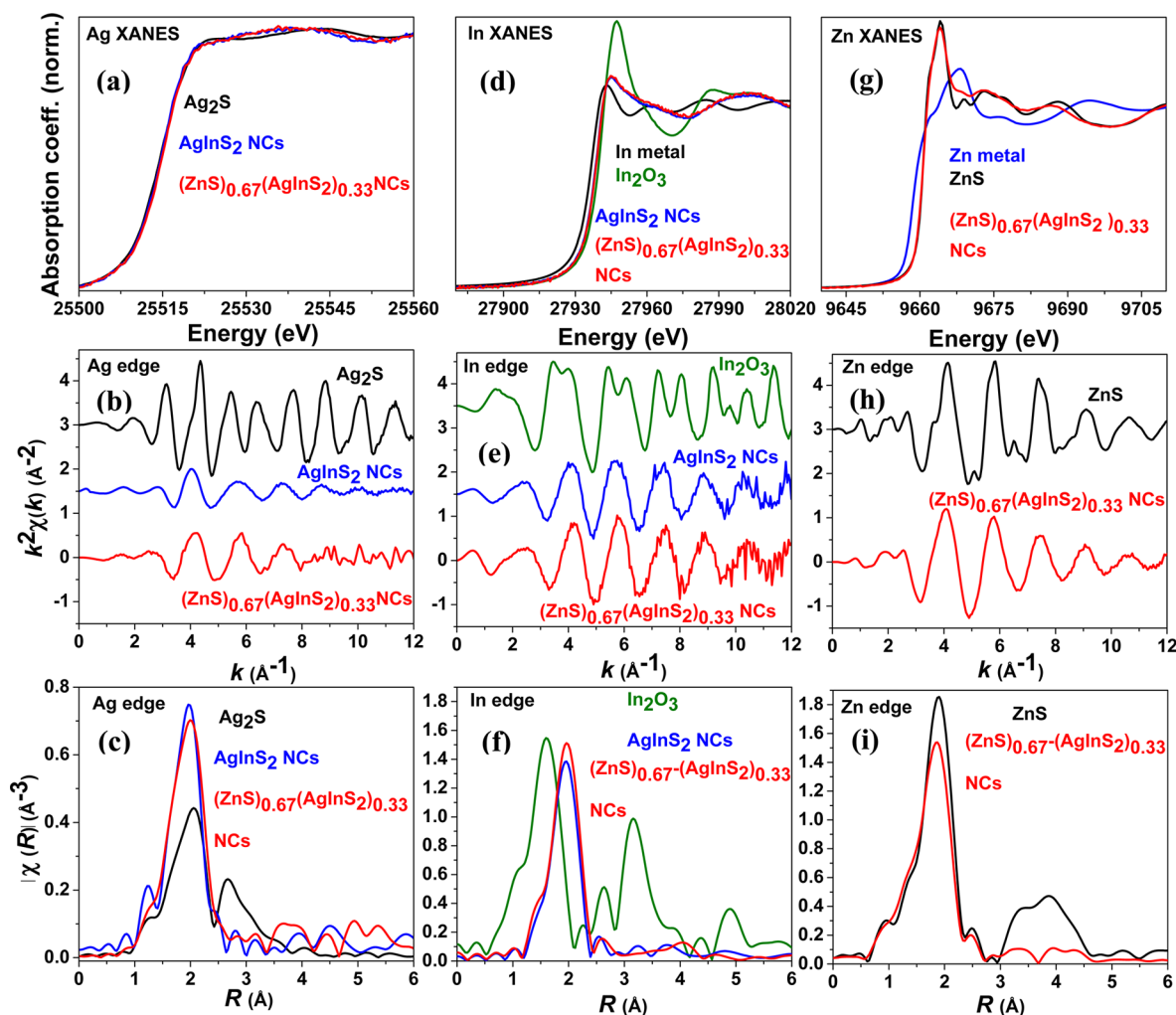


Figure 4. (a–c) Ag K-edge data for bulk Ag_2S standard, AgInS_2 NCs, and $(\text{ZnS})_{0.67}(\text{AgInS}_2)_{0.33}$ NCs: (a) XANES, (b) k^2 -weighted $\chi(k)$ data, and (c) magnitude of Fourier transformed data in R -space. (d–f) In K-edge data: (d) XANES, (e) k^2 -weighted $\chi(k)$ data, and (f) magnitude of Fourier-transformed data in R -space for NC samples and bulk standards. (g–i) Zn K-edge data for ZnS - AgInS_2 NCs and bulk standards: (g) XANES, (h) k^2 -weighted $\chi(k)$ data, and (i) magnitude of Fourier-transformed data in R -space. k^2 -weighted $\chi(k)$ data for AgInS_2 NCs in (b) and (e) have been shifted vertically by 1.5 for a better representation. Likewise, data for Ag_2S , In_2O_3 , and ZnS in (b), (e) and (h) have been shifted vertically by 3, 3.5, and 3, respectively.

emission features. It is to be noted that although the majority of I–III–VI₂ NCs reports suggest the D–A pair transition as the origin of PL,¹⁹ some reports^{18,23,31} also suggested Path-1 type transitions in CuInS_2 and CuInSe_2 NCs.

It has been commonly observed that for a given sample of $(\text{ZnS})_{1-x}(\text{AgInS}_2)_x$ NCs, the PL decay at the lower energy end of the spectrum is slower, as shown in Figure S1 of the SI. Such inhomogeneous lifetimes at different energies of a given spectrum can also be explained within our model, considering contributions from both Path-1 and Path-2 (D–A pair) in Figure 2. The blue shift in PL observed for AgInS_2 NCs with increasing excitation intensity shown in ref 24 can also be explained within our model. Lower energy transition Path-2 with longer lifetime saturates faster with increasing excitation intensity compared with Path-1 having a shorter lifetime, therefore, effectively increasing the higher energy Path-1 contribution at higher excitation intensity.

Next, we discuss the structural aspect of $(\text{ZnS})_{1-x}(\text{AgInS}_2)_x$ NCs. XRD patterns in Figure S2 of SI show a systematic shift of peak position toward higher 2θ values, similar to a previous report,²⁸ indicating the contraction of the lattice parameters

with the incorporation of ZnS. The broad nature of XRD pattern makes it difficult to distinguish between chalcopyrite and zinc-blende structure of $(\text{ZnS})_{1-x}(\text{AgInS}_2)_x$ NCs, which makes the application of Vegard's law³² of alloy formation somewhat uncertain. This XRD shift is also accompanied by a systematic blue shift in absorption spectra with the incorporation of ZnS, suggesting the formation of $(\text{ZnS})_{1-x}(\text{AgInS}_2)_x$ solid solution. However, the formation of smaller AgInS_2 core in $\text{AgInS}_2/\text{ZnS}$ core/shell NCs with increase in ZnS precursor cannot be excluded completely.³³

We carried out the XAFS study on $(\text{ZnS})_{1-x}(\text{AgInS}_2)_x$ NCs to elucidate the local structure. Zn K edge (9658 eV), Ag K edge (25514 eV), and In K edge (27940 eV) were measured using high-brilliance synchrotron radiation at 10ID in Advanced Photon Source, Argonne National Laboratory. The extended X-ray absorption fine structure (EXAFS) data were processed using Athena³⁴ by extracting the EXAFS oscillations $\chi(k)$ as a function of photoelectron wavenumber k following standard procedures.³⁵ The theoretical paths were generated using FEFF6 code implemented in Artemis fitting software.³⁴ The real (R) space data $\chi(R)$ were obtained by a Fourier transform

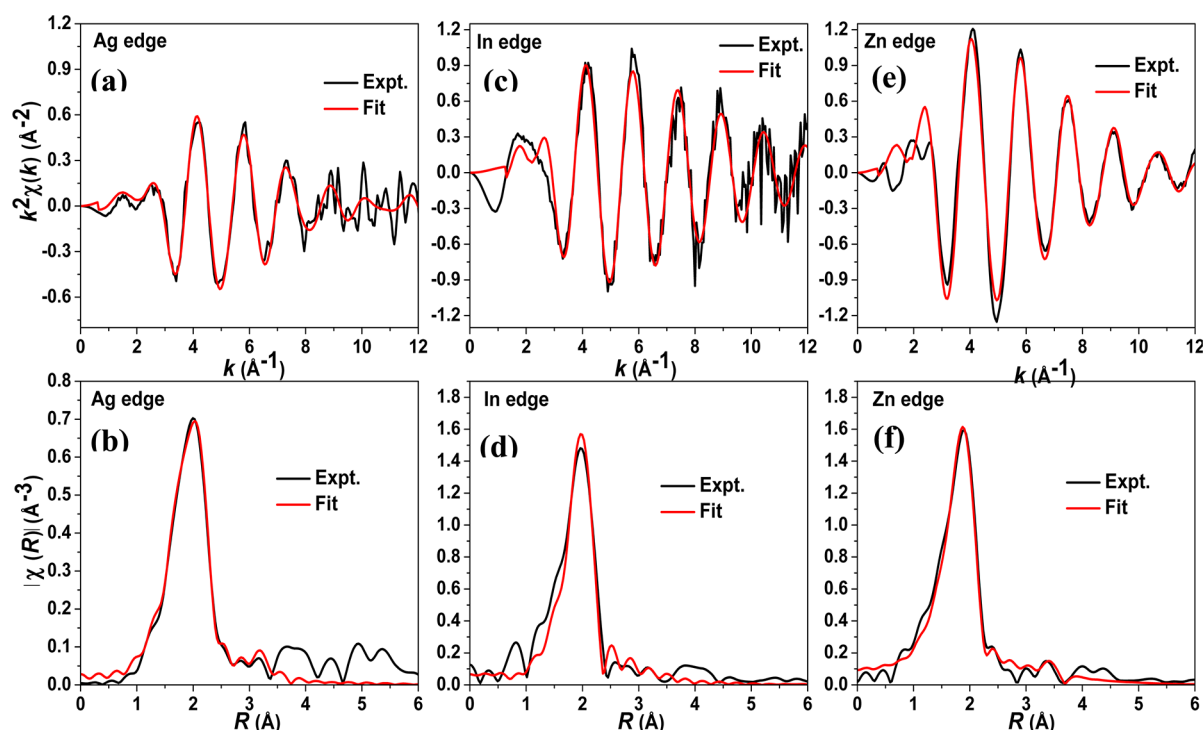


Figure 5. Fitting of k^2 -weighted $\chi(k)$ data and magnitude of Fourier-transformed data in R -space for Ag (a,b), In (c,d), and Zn (e,f) for $(\text{ZnS})_{0.67}(\text{AgInS}_2)_{0.33}$ NCs. R space data $\tilde{\chi}(R)$ is obtained by Fourier transform of k^2 -weighted $\chi(k)$ data, where $k = 2-11 \text{ \AA}^{-1}$ was transformed. In both k space and R space data, most of the contributions are from the first neighbors, and features from the farther neighbors (faster oscillations in $\chi(k)$) are very small. Thus the data were fitted only for the first nearest neighbor. Note that due to the photoelectron phase shift (ϕ_i), the Fourier peaks appear at shorter distance than the actual bond lengths.

of k^2 -weighted $\chi(k)$. Details of XAFS experiments and analysis are given in the SI. XAFS data of Ag K-edge, In K-edge, and Zn K-edge for $(\text{ZnS})_{1-x}(\text{AgInS}_2)_x$ NCs ($x = 1$ and 0.33) along with different bulk standards are shown in Figure 4a–c, Figure 4d–f, and Figure 4g–i, respectively. Data for both ($x = 1$ and 0.33) NC samples were fitted, and representative fits for $(\text{ZnS})_{0.67}(\text{AgInS}_2)_{0.33}$ NCs for all three edges are shown in Figure 5. The obtained best-fit parameters for both NC samples are tabulated in Table S2 of SI.

Figure 4a shows that Ag K-edge X-ray absorption near-edge structure (XANES) of both $(\text{ZnS})_{1-x}(\text{AgInS}_2)_x$ NC samples with $x = 1$ and 0.33 are similar to each other, and also the edge energy is similar to that of reference Ag_2S , suggesting the Ag is in the $1+$ oxidation state in our NCs. However, Ag_2S has somewhat different features compared with our NCs, owing to different structural aspects.³⁶ $\chi(R)$ for Ag-edge in Figure 4c shows only one peak corresponding to one Ag–S bond length, clearly different from the standard Ag_2S , which shows the existence of different Ag–S bond lengths similar to a previous report.³⁶ The fitting of k^2 -weighted $\chi(k)$ and R -space data (Figure 5a,b; Table S2 in the SI) show that the nearest-neighbor Ag–S bond length for both $(\text{ZnS})_{1-x}(\text{AgInS}_2)_x$ NCs is $\sim 2.52 \text{ \AA}$, similar to bulk³⁷ AgInS_2 . The coordination number (CN) for Ag–S is slightly smaller than the ideal CN of 4 expected from chalcopyrite or orthorhombic structure, both with tetrahedral coordination. This small decrease in CN is probably due to surface termination of NCs, where the metal ions do not have MS_4 tetrahedron.³⁸ The second nearest-neighbor Ag–S–metal correlation is weak for both of the NC samples.

In-edge energies of XANES (Figure 4d) of NC samples are similar to that of In_2O_3 and different from that of In metal,

suggesting that In is in $3+$ oxidation state in our NCs. k^2 -weighted $\chi(k)$ (Figure 4e) and R -space (Figure 4f) In-edge data are similar for both NC samples and are clearly different from the standard In_2O_3 . R -space data show the longer nearest-neighbor In–S bond in NCs compared with the In–O bond lengths, suggesting the absence of any unwanted oxide formation; also, second nearest-neighbor correlation is present in the standard In_2O_3 but absent in our NC samples. Fitting (Figure 5c,d) of k^2 -weighted $\chi(k)$ and R -space data show that the nearest-neighbor In–S bond length for both $(\text{ZnS})_{1-x}(\text{AgInS}_2)_x$ NC samples is about 2.45 \AA , with CN slightly lower than the ideal tetrahedral coordination. The smaller InS_4 tetrahedra (In–S bond length 2.45 \AA) compared with AgS_4 tetrahedra (Ag–S bond length 2.52 \AA) is because of the smaller ionic radius of tetrahedral In^{3+} compared with that of tetrahedral Ag^+ .³⁹ S is expected to be surrounded by two Ag and two In, so the second nearest-neighbor metal–S–metal correlation is not expected to be prominent in the EXAFS of solid-solution NCs. Furthermore, the large surface/volume ratio of our NCs can contribute to the blurring of the second nearest-neighbor correlation.

Zn-edge XANES data for $(\text{ZnS})_{0.67}(\text{AgInS}_2)_{0.33}$ NCs in Figure 4g show that Zn is in $2+$ oxidation state similar to reference ZnS. However, reference ZnS shows a distinct feature at $\sim 9668.7 \text{ eV}$, which got blurred for $(\text{ZnS})_{0.67}(\text{AgInS}_2)_{0.33}$ NCs. Similarly, R -space data (Figure 4i) for Zn-edge also show the absence of Zn–S–Zn second nearest-neighbor correlation for $(\text{ZnS})_{0.67}(\text{AgInS}_2)_{0.33}$ NCs of $\sim 4 \text{ \AA}$, which is clearly visible for reference ZnS. Owing to small size, NC samples typically do not show second neighbor correlations; however, some NCs can show such correlations. Thus the complete absence of second nearest-neighbor correlations in our

(ZnS)_{0.67}(AgInS₂)_{0.33} NCs may not be solely because of the size effect but also because of the random occupation of the second neighbor sites by Zn, Ag, and In, suggesting the formation of solid solution. Fitting (Figure 5e,f) of k^2 -weighted $\chi(k)$ and R -space data yields Zn–S bond length of 2.33 Å, similar to that of ZnS reference (2.35 Å), and is smaller than that of both Ag–S (2.52 Å) and In–S (2.45 Å). The similarity in nearest-neighbor (Zn–S) bond length between the solid solution and the end-member ZnS is rather commonly observed fact.⁴⁰

PL depends on very small concentration of defects. On the other end, structural investigations based on XRD, high-resolution TEM, and EXAFS can be insensitive to probe defects at such smaller concentrations. However, our EXAFS results, in combination with XRD and UV–visible data, agree with the formation of (ZnS)_{1-x}(AgInS₂)_x solid solution NCs. Our detailed structural investigation showing no detectable phase separated products further builds the confidence of our PL analysis. In AgInS₂ NCs, defects can originate from different bonding nature of Ag–S and In–S, and typical defects can be Ag vacancy/interstitial, sulfur vacancy/interstitial, In in the place of Ag, or vice versa. Unfortunately, so far, not much is known about the exact nature of defects in AgInS₂ NCs that is responsible for PL transitions. Incorporation of Zn in the lattice has been reported to reduce some of these defect densities,¹⁰ which might reduce the contribution of Path-2 with increasing ZnS content. Another possibility is that as the energy difference between defects states and valence/conduction band increases with incorporation of ZnS, nonradiative relaxation of electron or hole to the respective defect states can be slower requiring multiphonon processes,⁴¹ thereby reducing the contribution from Path-2.

In conclusion, (ZnS)_{1-x}(AgInS₂)_x NCs allowed us to change the band gap simply by changing the composition but without changing the size of the NCs (~5 nm). Therefore, if the luminescence mechanism is D–A pair transition, as suggested previously, the D–A pair distance is expected to be the same for all NC samples with different x and is anticipated to exhibit similar emission energy and lifetime. In sharp contrast, we observe a systematic change in PL peak position that is quantitatively comparable to the change in band gap with composition x , and also the PL decay is significantly faster for smaller x . Furthermore, the PL peak blue-shifts by 0.57 eV, which is too high to be explained by any change in D–A pair Coulomb interaction energy. Clearly, these experimental observations cannot be explained by previously assigned D–A pair transition; instead, we put forward a new light-emission mechanism that has contributions from two paths. Path-1 involves delocalized valence/conduction band and localized defect states exhibiting higher emission energy with smaller lifetime (~25 ns), and Path-2 involves two localized donor and acceptor states with lower emission energy and longer lifetime (>185 ns). Contribution from Path-1 increases systematically with decreasing x , and in fact for $x = 0.33$, the emission is mostly governed by Path-1. This large contribution from Path-1 can explain the large (0.57 eV) and systematic blue shift in PL spectra, similar to the change in band gap, with composition x . XANES and EXAFS results for Ag K-edge, In K-edge, and Zn K-edge elucidate the local structure of (ZnS)_{1-x}(AgInS₂)_x NCs for the first time for all $x > 0$. Nearest-neighbor Ag–S and In–S bond lengths were found to be 2.52 and 2.45 Å, respectively, for AgInS₂ ($x = 1$) NCs and solid solutions having tetrahedral coordination. Zn–S bond length is found to be 2.33 Å for

(ZnS)_{0.67}(AgInS₂)_{0.33} NCs, with no second nearest-neighbor Zn–S–metal correlation.

■ ASSOCIATED CONTENT

Supporting Information

Detailed experimental sections, XAFS analysis, PL decays, and XRD. This material is available free of charge via the Internet at <http://pubs.acs.org>.

■ AUTHOR INFORMATION

Corresponding Author

*E-mail: angshuman@iiserpune.ac.in.

Notes

The authors declare no competing financial interest.

■ ACKNOWLEDGMENTS

We thank the Director of IISER Pune for financial support and encouragement. A.N. acknowledges Department of Science and Technology (DST) for Ramanujan Fellowship and DAE-BRNS grant (2013/20/37C/1/BRNS/954) Govt. of India. We thank Nanoscience Unit Grant (SR/NM/NS-42/2009) of DST, Govt. of India. M.J.R. acknowledges CSIR, Govt. of India, for a junior research fellowship. MRCAT operations are supported by the Department of Energy and MRCAT host institutions. Use of the Advanced Photon Source is supported by the U.S. Department of Energy, Office of Science, Office of Basic Energy Sciences, under contract no. DE-AC02-06CH11357.

■ REFERENCES

- (1) Tsuji, I.; Kato, H.; Kobayashi, H.; Kudo, A. Photocatalytic H₂ Evolution Reaction from Aqueous Solutions over Band Structure-Controlled (AgIn)_xZn_{2(1-x)}S₂ Solid Solution Photocatalysts with Visible-Light Response and their Surface Nanostructures. *J. Am. Chem. Soc.* **2004**, *126*, 13406–13413.
- (2) Peng, S. J.; Zhang, S. Y.; Mhaisalkar, S. G.; Ramakrishna, S. Synthesis of AgInS₂ Nanocrystal Ink and its Photoelectrical Application. *Phys. Chem. Chem. Phys.* **2012**, *14*, 8523–8529.
- (3) Sasamura, T.; Okazaki, K.; Kudo, A.; Kuwabata, S.; Torimoto, T. Photosensitization of ZnO Rod Electrodes with AgInS₂ Nanoparticles and ZnS-AgInS₂ Solid Solution Nanoparticles for Solar Cell Applications. *RSC Adv.* **2012**, *2*, 552–559.
- (4) Guchhait, A.; Pal, A. J. Copper-Diffused AgInS₂ Ternary Nanocrystals in Hybrid Bulk-Heterojunction Solar Cells: Near-Infrared Active Nanophotovoltaics. *ACS Appl. Mater. Interfaces* **2013**, *5*, 4181–4189.
- (5) Takahashi, T.; Kudo, A.; Kuwabata, S.; Ishikawa, A.; Ishihara, H.; Tsuboi, Y.; Torimoto, T. Plasmon-Enhanced Photoluminescence and Photocatalytic Activities of Visible-Light-Responsive ZnS-AgInS₂ Solid Solution Nanoparticles. *J. Phys. Chem. C* **2013**, *117*, 2511–2520.
- (6) Uematsu, T.; Doko, A.; Torimoto, T.; Oohora, K.; Hayashi, T.; Kuwabata, S. Photoinduced Electron Transfer of ZnS–AgInS₂ Solid-Solution Semiconductor Nanoparticles: Emission Quenching and Photocatalytic Reactions Controlled by Electrostatic Forces. *J. Phys. Chem. C* **2013**, *117*, 15667–15676.
- (7) Deng, M. J.; Shen, S. L.; Wang, X. W.; Zhang, Y. J.; Xu, H. R.; Zhang, T.; Wang, Q. B. Controlled Synthesis of AgInS₂ Nanocrystals and Their Application in Organic–Inorganic Hybrid Photodetectors. *CrystEngComm* **2013**, *15*, 6443–6447.
- (8) Torimoto, T.; Ogawa, S.; Adachi, T.; Kameyama, T.; Okazaki, K. I.; Shibayama, T.; Kudo, A.; Kuwabata, S. Remarkable Photoluminescence Enhancement of ZnS–AgInS₂ Solid Solution Nanoparticles by Post-Synthesis Treatment. *Chem. Commun.* **2010**, *46*, 2082–2084.
- (9) Chang, J. Y.; Wang, G. Q.; Cheng, C. Y.; Lin, W. X.; Hsu, J. C. Strategies for Photoluminescence Enhancement of AgInS₂ Quantum

Dots and their Application as Bioimaging Probes. *J. Mater. Chem.* **2012**, *22*, 10609–10618.

(10) Tang, X. S.; Ho, W. B. A.; Xue, J. M. Synthesis of Zn-Doped AgInS₂ Nanocrystals and Their Fluorescence Properties. *J. Phys. Chem. C* **2012**, *116*, 9769–9773.

(11) Manna, G.; Jana, S.; Bose, R.; Pradhan, N. Mn-Doped Multinary CIZS and AIZS Nanocrystals. *J. Phys. Chem. Lett.* **2012**, *3*, 2528–2534.

(12) Murray, C. B.; Norris, D. J.; Bawendi, M. G. Synthesis and Characterization of Nearly Monodisperse CdE (E = S, Se, Te) Semiconductor Nanocrystallites. *J. Am. Chem. Soc.* **1993**, *115*, 8706–8715.

(13) Talapin, D. V.; Nelson, J. H.; Shevchenko, E. V.; Aloni, S.; Sadtler, B.; Alivisatos, A. P. Seeded Growth of Highly Luminescent CdSe/CdS Nanoheterostructures with Rod And Tetrapod Morphologies. *Nano Lett.* **2007**, *7*, 2951–2959.

(14) Dias, E. A.; Sewall, S. L.; Kambhampati, P. Light Harvesting and Carrier Transport in Core/Barrier/Shell Semiconductor Nanocrystals. *J. Phys. Chem. C* **2007**, *111*, 708–713.

(15) Santra, P. K.; Kamat, P. V. Tandem-Layered Quantum Dot Solar Cells: Tuning the Photovoltaic Response with Luminescent Ternary Cadmium Chalcogenides. *J. Am. Chem. Soc.* **2013**, *135*, 877–885.

(16) Saha, A.; Chellappan, K. V.; Narayan, K. S.; Ghatak, J.; Datta, R.; Viswanatha, R. Near-Unity Quantum Yield in Semiconducting Nanostructures: Structural Understanding Leading to Energy Efficient Applications. *J. Phys. Chem. Lett.* **2013**, *4*, 3544–3549.

(17) Xie, R. G.; Rutherford, M.; Peng, X. G. Formation of High-Quality I-III-VI Semiconductor Nanocrystals by Tuning Relative Reactivity of Cationic Precursors. *J. Am. Chem. Soc.* **2009**, *131*, 5691–5697.

(18) Li, L. A.; Pandey, A.; Werder, D. J.; Khanal, B. P.; Pietryga, J. M.; Klimov, V. I. Efficient Synthesis of Highly Luminescent Copper Indium Sulfide-Based Core/Shell Nanocrystals with Surprisingly Long-Lived Emission. *J. Am. Chem. Soc.* **2011**, *133*, 1176–1179.

(19) Zhong, H. Z.; Bai, Z. L.; Zou, B. S. Tuning the Luminescence Properties of Colloidal I-III-VI Semiconductor Nanocrystals for Optoelectronics and Biotechnology Applications. *J. Phys. Chem. Lett.* **2012**, *3*, 3167–3175.

(20) Pradhan, N.; Goorskey, D.; Thessing, J.; Peng, X. G. An Alternative of CdSe Nanocrystal Emitters: Pure and Tunable Impurity Emissions in ZnSe Nanocrystals. *J. Am. Chem. Soc.* **2005**, *127*, 17586–17587.

(21) Nag, A.; Chakraborty, S.; Sarma, D. D. To dope Mn²⁺ in a Semiconducting Nanocrystal. *J. Am. Chem. Soc.* **2008**, *130*, 10605–10611.

(22) Hazarika, A.; Layek, A.; De, S.; Nag, A.; Debnath, S.; Mahadevan, P.; Chowdhury, A.; Sarma, D. D. Ultranarrow and Widely Tunable Mn²⁺-Induced Photoluminescence from Single Mn-Doped Nanocrystals of ZnS-CdS Alloys. *Phys. Rev. Lett.* **2013**, *110*, 267401.

(23) Tan, Z. N.; Zhang, Y.; Xie, C.; Su, H. P.; Liu, J.; Zhang, C. F.; Dellas, N.; Mohny, S. E.; Wang, Y. Q.; Wang, J. K.; Xu, J. Near-Band-Edge Electroluminescence from Heavy-Metal-Free Colloidal Quantum Dots. *Adv. Mater.* **2011**, *23*, 3553–3558.

(24) Ogawa, T.; Kuzuya, T.; Hamanaka, Y.; Sumiyama, K. Synthesis of Ag-In Binary Sulfide Nanoparticles-Structural Tuning and Their Photoluminescence Properties. *J. Mater. Chem.* **2010**, *20*, 2226–2231.

(25) Hamanaka, Y.; Ogawa, T.; Tsuzuki, M.; Kuzuya, T. Photoluminescence Properties and its Origin of AgInS₂ Quantum Dots with Chalcopyrite Structure. *J. Phys. Chem. C* **2011**, *115*, 1786–1792.

(26) Rockenberger, J.; Troger, L.; Kornowski, A.; Vossmeier, T.; Eychmüller, A.; Feldhaus, J.; Weller, H. EXAFS Studies on the Size Dependence of Structural and Dynamic Properties of CdS Nanoparticles. *J. Phys. Chem. B* **1997**, *101*, 2691–2701.

(27) Nag, A.; Kumar, A.; Kiran, P. P.; Chakraborty, S.; Kumar, G. R.; Sarma, D. D. Optically Bifunctional Heterostructured Nanocrystals. *J. Phys. Chem. C* **2008**, *112*, 8229–8233.

(28) Torimoto, T.; Adachi, T.; Okazaki, K.; Sakuraoaka, M.; Shibayama, T.; Ohtani, B.; Kudo, A.; Kuwabata, S. Facile Synthesis

of ZnS-AgInS₂ Solid Solution Nanoparticles for a Color-Adjustable Luminophore. *J. Am. Chem. Soc.* **2007**, *129*, 12388–12389.

(29) Mao, B. D.; Chuang, C. H.; Wang, J. W.; Burda, C. Synthesis and Photophysical Properties of Ternary I-III-VI AgInS₂ Nanocrystals: Intrinsic versus Surface States. *J. Phys. Chem. C* **2011**, *115*, 8945–8954.

(30) Shay, J. L.; Tell, B.; Schiavon, L. M.; Kasper, H. M.; Thiel, F. Energy-Bands of AgInS₂ in Chalcopyrite and Orthorhombic Structures. *Phys. Rev. B* **1974**, *9*, 1719–1723.

(31) Nose, K.; Omata, T.; Otsuka-Yao-Matsuo, S. Colloidal Synthesis of Ternary Copper Indium Diselenide Quantum Dots and Their Optical Properties. *J. Phys. Chem. C* **2009**, *113*, 3455–3460.

(32) Vegard, L. Die Konstitution der Mischkristalle und die Raumfüllung der Atome. *Z. Phys.* **1921**, *5*, 17–26.

(33) Yang, X.; Tang, Y.; Tan, S. T.; Bosman, M.; Dong, Z.; Leck, K. S.; Ji, Y.; Demir, H. V.; Sun, X. W. Facile Synthesis of Luminescent AgInS₂-ZnS Solid Solution Nanorods. *Small* **2013**, *9*, 2689–2695.

(34) Ravel, B.; Newville, M. J. ATHENA, ARTEMIS, HEPHAESTUS: Data Analysis For X-Ray Absorption Spectroscopy Using IFEFFIT. *Synchrotr. Radiat* **2005**, *12*, 537–541.

(35) *X-ray Absorption, Principles, Applications, Techniques of EXAFS, SEXAFS and XANES*; Korningsberger, D. C.; Prins, R., Eds.; John Wiley & Sons: New York, 1988.

(36) Kashida, S.; Watanabe, N.; Hasegawa, T.; Iida, H.; Mori, M.; Savrasov, S. Electronic Structure of Ag₂S, Band Calculation and Photoelectron Spectroscopy. *Solid State Ionics* **2003**, *158*, 167–175.

(37) Delgado, G.; Mora, A. J.; Pineda, C.; Tinoco, T. Simultaneous Rietveld Refinement of Three Phases in the Ag-In-S semiconducting System from X-ray Powder Diffraction. *Mater. Res. Bull.* **2001**, *36*, 2507–2517.

(38) Nag, A.; Chung, D. S.; Dolzhenkov, D. S.; Dimitrijevic, N. M.; Chattopadhyay, S.; Shibata, T.; Talapin, D. V. Effect of Metal Ions on Photoluminescence, Charge Transport, Magnetic and Catalytic Properties of All-Inorganic Colloidal Nanocrystals and Nanocrystal Solids. *J. Am. Chem. Soc.* **2012**, *134*, 13604–13615.

(39) Shannon, R. D. Revised Effective Ionic-Radii and Systematic Studies of Interatomic Distances in Halides And Chalcogenides. *Acta Crystallogr., Sect. A* **1976**, *32*, 751–767.

(40) Santangelo, S. A.; Hinds, E. A.; Vlaskin, V. A.; Archer, P. I.; Gamelin, D. R. Bimodal Bond-Length Distributions in Cobalt-Doped CdSe, ZnSe, and Cd_{1-x}Zn_xSe Quantum Dots. *J. Am. Chem. Soc.* **2007**, *129*, 3973–3978.

(41) Cooney, R. R.; Sewall, S. L.; Anderson, K. E. H.; Dias, E. A.; Kambhampati, P. Breaking the Phonon Bottleneck for Holes in Semiconductor Quantum Dots. *Phys. Rev. Lett.* **2007**, *98*, 177403.